Piezoelectric sensor characterization in buckling mode for structural dynamic strain measurements

Ghaderiaram, Aliakbar; Schlangen, Erik; Fotouhi, Mohammad

DOI
10.1016/j.snr.2025.100362

Publication date
2025

Document Version
Final published version

Published in
Sensors and Actuators Reports

Sensors and Actuators Reports 10 (2025) 100362

Contents lists available at ScienceDirect

Sensors and Actuators Reports

journal homepage: www.sciencedirect.com/journal/sensors-and-actuators-reports

Piezoelectric sensor characterization in buckling mode for structural dynamic strain measurements

Aliakbar Ghaderiaram *, Erik Schlangen, Mohammad Fotouhi

The Delft University of Technology, Delft, Netherlands

ARTICLE INFO

Keywords:
Piezoelectric
Buckling
Dynamic strain
Modelling
Optimisation

ABSTRACT

The buckling mode in piezoelectric materials offers advantages such as an increased measurable strain range, ease of installation, and extended service life. This paper investigates the potential of piezoelectric sensors operating in buckling mode for structural strain measurement by evaluating key factors including boundary conditions, sensor response linearity under dynamic loading, and impedance engineering to optimize the voltage–strain relationship. A structural extension was developed to facilitate sensor integration and to enable the application of different buckling boundary conditions. Results show that the clamped–clamped configuration generated at least 1.65 times higher output voltage, and three times greater peak strain compared to other boundary conditions. An experimentally validated analytical model was employed to assess and improve the performance of buckled piezoelectric sensors in dynamic environments. The findings highlight that introducing initial buckling reduces signal perturbations, enhances voltage linearity across loading frequencies, and extends the effective strain measurement range. Furthermore, impedance engineering was used to successfully mitigate the nonlinear effects of transient response, thereby improving signal stability and accuracy in dynamic strain monitoring applications.

1. Introduction

Dynamic strain monitoring is widely used to evaluate structural integrity, characterize dynamic behaviour, and estimate the service life of engineering structures [1–3]. Hence, strain sensors are increasingly applied for dynamic strain measurement and structural health monitoring (SHM). Foil strain gauges (SGs) have been commonly utilized for strain detection; however, their performance can be affected by electrical noise and limited dynamic response sensitivity [4,5]. Additional challenges include calibration challenges and reduced high-frequency sensitivity due to small deformation amplitudes [6].

Fiber Bragg grating sensors are a promising alternative for strain measurement due to their high sensitivity, lightweight design, and immunity to electromagnetic interference [7–10]. However, limitations include thermal sensitivity, fragility, and potential long-term signal degradation [11,12]. Additionally, their interrogation systems can be costly, particularly for high-frequency monitoring applications [13].

Piezoresistive strain sensors have been studied for their simplicity and material versatility [14,15], they are primarily suited for static or low-frequency applications [16,17]. In contrast, piezoelectric strain sensors are better suited for dynamic monitoring, as they generate electrical charge in response to strain rate, enabling self-powered operation, high signal fidelity, and broad frequency response [18,19].

Piezoelectric strain sensors convert mechanical strain into electrical charges, enabling them to detect even minute, rapid strain variations [20]. They are cost-effective, offer a wide frequency range, and are compatible with common signal conditioning and data collection systems [21,22]. These sensors are known for their fast dynamic response, high sensitivity, low signal decay, long fatigue life, and durability in operational conditions, making them widely used in various applications [23,24]. Mainly, two types of piezoelectric materials are employed in sensor design, such as lead zirconate titanate (PZT) and polyvinylidene fluoride (PVDF), each optimized for specific uses [25].

Strain measurement in piezoelectric sensors is restricted to the linear region in the piezoelectric material response against the strain, limiting their application for high-strain level measurements, such as high-strain to failure materials or joints, where large strains may occur [18]. In our previous study, a comprehensive analytical and experimental investigation was done for applying piezoelectric sensors for structural strain measurement, considering the attachment strategy and mechanical

* Corresponding author.
E-mail address: a.ghaderiaram@tudelft.nl (A. Ghaderiaram).

https://doi.org/10.1016/j.snr.2025.100362
Received 18 March 2025; Received in revised form 14 July 2025; Accepted 21 July 2025
Available online 22 July 2025

Table 1
Piezoelectric sensor and the test structure's properties [40–42].

Property	Qty	Unit
Min. lateral contraction (PZT)	650	$\mu m/m$
Min. bending radius	12	mm
Electrical capacitance	150	nF
Poisson ratio (PZT)	0.35	
Young's moduli E_1=E_2 (PIC255)	63E9	Nm^{-2}
Young's modulus (PZT sensor)	16.4E9	Nm^{-2}
$e_{31} = e_{32}$ (PZT)	−4.51	Cm^{-2}
e_{33} (PZT)	17.22	Cm^{-2}
Permittivity at constant strain (PIC255)	8.23E-9	Fm^{-1}
Young's modulus (aluminum)	7.04E10	Nm^{-2}
Yield strength (aluminum)	3.09E8	Nm^{-2}

properties of the structure that is being monitored [26]. The results, alongside a review of existing studies, highlighted certain limitations, such as the strain measurement range being constrained to 100–150 με due to material nonlinearities [27,28]. Other experimental findings reported maximum strain limits of 1 to 3.5 % [29,30] and strong dependency of the measured values on factors like the test structure and the bonding quality.

Recent developments in flexible strain sensors have improved the balance between large strain range and high sensitivity through advanced materials and structural designs [31,32]. While promising for wearable and soft robotics applications, their use in structural monitoring is limited due to integration and durability challenges [33].

To tackle the measurable strain range limit, piezoelectric sensors can be utilized in a buckling mode, where the initial buckling (IB) chord determines the maximum measurable displacement [34]. Additionally, buckled shapes may be more suitable for curved structures or offer installation flexibility for hard-to-access areas such as joints. While studies in the literature have explored the use of piezoelectric films in buckling mode, the primary focus has been energy harvesting. For instance, C. Dagdeviren et al. designed and fabricated a network of PZT-based piezoelectric sensors on a thin polyimide layer, creating a biocompatible system to harvest heart movements in buckling mode [35]. Similarly, F. Cottone et al. conducted an analytical and experimental study using piezoelectric sensors in buckling mode to harvest energy from random vibrations, correlating the vibration characteristics with the sensor's output [36]. J. Chen et al. investigated piezoelectric generators through numerical and experimental analyses of thin PZT layers on flexible substrates under buckling conditions. Their work also detailed the equivalent circuit of the piezoelectric sensor [37]. A common thread across these studies is the consistent use of specific boundary conditions and approaches for strain distribution calculations, as thoroughly outlined in the work by J. Song et al. [38].

To summarize, while piezoelectric sensors have shown potential in buckling mode applications, most existing literature primarily focuses on energy harvesting, especially on curved surfaces, rather than on structural strain measurement. A significant knowledge gap remains in evaluating key factors such as buckling boundary conditions and the linearity of sensor responses under dynamic strains. These aspects, crucial for the reliable use of piezoelectric sensors in strain monitoring, have not been explored so far. Addressing this gap is essential to fully leverage the capabilities of piezoelectric sensors for dynamic strain measurement and to advance their use in SHM. This study addresses this gap by presenting an experimentally validated analytical investigation of the piezoelectric electromechanical behavior in buckling mode. While much of the existing research has focused on clamped–clamped (CC) boundary conditions, this work explores a wider range of conditions and

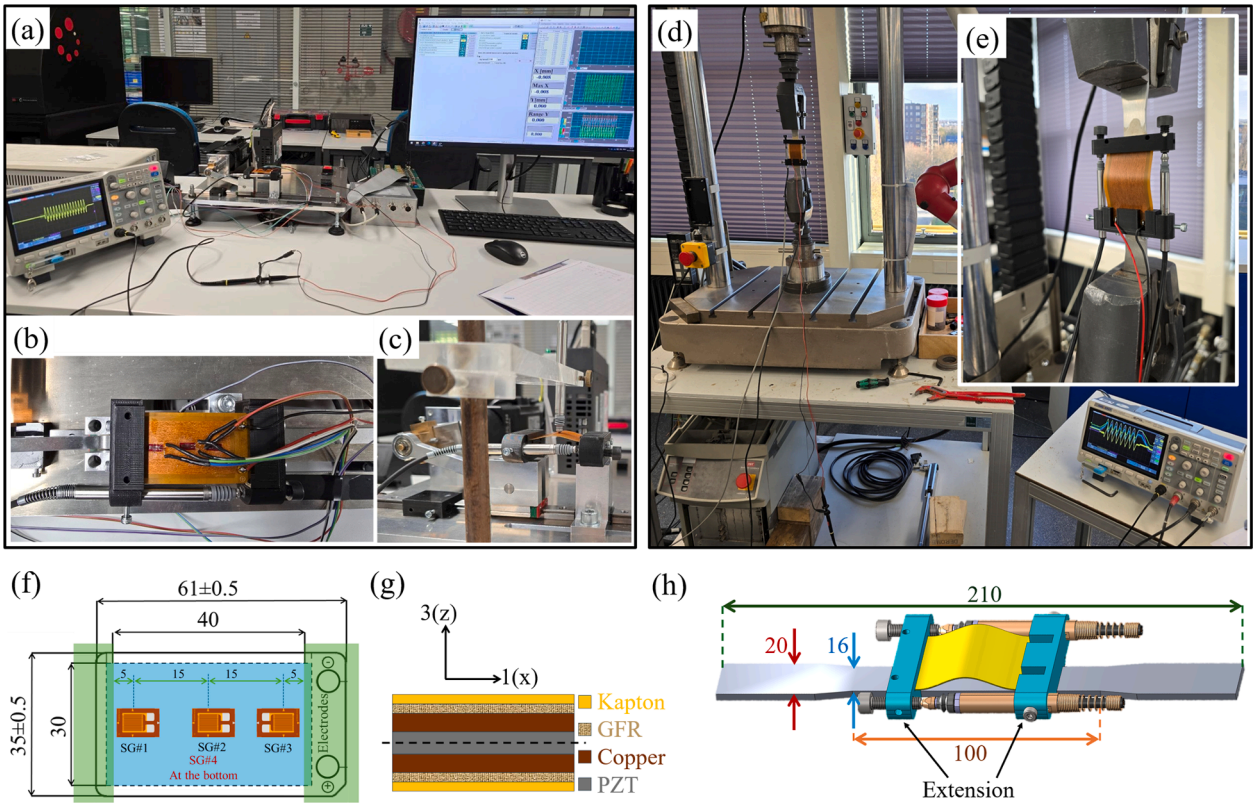

Fig. 1. (a) Test setup for buckling mode boundary condition experiments, (b) displays the piezoelectric sensor with the SGs installed, (c) illustrates the setup used to capture the deflection profile during buckling cycles, (d) test setup for cyclic tension-tension testing on the aluminum dog-bone specimen, (e) provides a close-up view of the buckled piezoelectric sensor installed on extension and LVDT placement, (f) shows the dimensions and the location of strain gauges, (g) represents the different layers of the piezoelectric sensor, (h) shows the schematic of the aluminum dog-bone test structure with the extension installation including LVDTs for tension-tension test (given dimensions are in mm).

offers a comprehensive analysis. Various experimental tests are conducted to validate theoretical results. To facilitate sensor installation, an extension is designed to address buckling boundary conditions and assist with sensor integration [39]. By optimizing key parameters such as boundary conditions, IB, and impedance, this study aims to design a piezoelectric sensor with improved linearity, minimizing perturbations and challenges in the voltage-strain relationship, and ultimately enhancing its reliability for structural strain measurements.

2. Materials and methods

Table 1 summarizes the key properties of the PZT piezoelectric sensor used in this study. The P-876.A11 sensor, as shown in Fig. 1(g), is fabricated from PIC255 piezo-ceramic material and produced by PI Company [40]. This is a 100 μm PZT layer sandwiched between ~75 μm copper electrodes, ~50 μm glass-fibre-reinforced (GFR) layers, and ~25 μm Kapton encapsulation layers on both sides. The test structure is a dog-bone-shaped specimen made of 6061-T6 aluminum with dimensions of 210 × 20 × 3 mm ($L \times W \times T$). A 3D-printed extension is attached to the test structure using an epoxy adhesive, ensuring a robust bonding for experimental testing.

Two experimental setups were developed to investigate the piezoelectric characteristics in buckling mode and evaluate the performance of a piezoelectric sensor installed on an aluminum dog-bone structure, as shown in Fig. 1. The developed extension enables either pinned or clamped boundary conditions: a free-rotation space creates a pinned condition, while a tight slot ensures a clamped condition. Fig. 1(a) shows a test machine providing reciprocating linear motion to vary the buckling chord and frequency for each condition, along with a linear variable differential transformer (LVDT) to measure the buckling chord. Fig. 1(c) illustrates an alternative configuration with two LVDTs capturing the sensor's deflection profile along the X and Z axes. Three SGs are mounted on the sensor's top surface, with one additional SG on the bottom surface directly beneath the middle strain gauge (SG#2), as depicted in Fig. 1(f).

For the tension-tension test, depicted in Fig. 1(d), an Instron machine is employed to apply a range of tensile load amplitudes and frequencies. A minimum preload of 0.5 kN is maintained throughout the test to ensure the clamps remain securely engaged. Maximum loads ranging from 2 to 8 kN are applied, ensuring the specimen remains within its linear elastic region. Additionally, 0.5 and 4 Hz loading frequencies are applied to each load amplitude. To verify uniform tension in the aluminum dog-bone specimen and accurately measure displacement, two LVDTs are positioned on both sides of the extension.

Adjusting the extension's initial positioning sets four different levels of IB, ranging from 0.5 to 2 mm. A range of load resistors from 10 to 100 kΩ is selected to investigate the linearity of the piezoelectric sensor's output. To record the piezoelectric sensor's output, as well as synchronized LVDT and force data, a digital oscilloscope operating at a sampling rate of 1 GS/s is utilized, ensuring high-fidelity signal acquisition.

3. Voltage-strain relationship in buckled piezoelectric sensor

Piezoelectric materials generate electric charge under mechanical stress and deform when subjected to an electric field, making them ideal for use in sensors and actuators [25]. Methodically considering thermodynamics and Maxwell's equations, Eq. (1) provides the relationship between the generated output voltage and mechanical strain in a PZT [25]. Piezoelectric materials can be broadly categorized into natural and synthetic types. Natural piezoelectric materials, such as quartz and tourmaline, exhibit inherent piezoelectric properties due to their crystalline structure

Eq. (1) is the *e*-form (stress-charge form) of the piezoelectric governing equation that describes the electromechanical behaviour of piezoelectric materials. The first term, D_m, represents the electrical displacement generated by mechanical stress, illustrating the sensor mode of the piezoelectric material. The second term, ε_{kl}, corresponds to the mechanical strain induced by an applied electric field, characterizing the actuator mode.

Table 2
The expressions used in Eq. (1).

Notation	Description	Unit
Intensive state variables		
$\boldsymbol{E_n}$	Electric field density; vector	Vm^{-1}
$\boldsymbol{T_{ij}}$	Mechanical stress; tensor rank 2	Nm^{-2}
Extensive state variables		
$\boldsymbol{D_m}$	Electric flux density; vector	Cm^2
$\boldsymbol{\varepsilon_{kl}}$	Mechanical strain; tensor rank 2	–
Material parameter		
$\boldsymbol{k^S_{mn}}$	Electric permittivity; tensor rank 2	$AsV^{-1}m^{-1}$; Fm^{-1}
$\boldsymbol{e_{mkl}}$	Piezoelectric stress constants; tensor rank 3	Cm^{-2}; NV^{-1} m^{-1}
$\boldsymbol{c^E_{ijkl}}$	Elastic compliance constants; tensor rank 4	m^2N^{-1}

$$\begin{aligned} D_m &= k^S_{mn}E_n + e_{mkl}\varepsilon_{kl} \\ T_{ij} &= -e_{ijn}E_n + c^E_{ijkl}\varepsilon_{kl} \end{aligned} \tag{1}$$

Where all the variables and material parameters are defined in Table 2. The superscripts of the material parameters point out which physical quantities are presumed to stay constant in the framework of parameter identification and the subscripts $\{i,\ j,\ k,\ l,\ m,\ n\}$ correspond to the spatial axes $\{x,\ y,\ z\}$ or $\{1,\ 2,\ 3\}$.

The first part of Eq. (1) is a summation of two terms. The term $k^S_{mn}E_n$ defines the electrical displacement resulting from the application of an electric field and the $e_{mkl}\varepsilon_{kl}$ the term is generated by mechanical strain. Since there is no external application of an electric field in this study, the former term can also be disregarded. Consequently, the most relevant equation linking mechanical strain to electrical displacement is expressed in Eq. (2).

$$D_m = e_{mkl}\varepsilon_{kl} \tag{2}$$

The equivalent circuit model of Van Dyke can be used to relate the output voltage to the electrical displacement [43,44]. This model can be simplified at lower loading frequencies [45], as shown in Fig. 2(a). Here, C represents the capacitance formed by the two parallel electrodes with the PZT material acting as the dielectric, R_P accounts for charge leakage or recombination, and R_L represents the impedance of the external circuit [37]. For further simplification, R_P and R_L can be combined into a single equivalent resistance, reducing the model to a first-order parallel RC circuit, as illustrated in Fig. 2(a).

The capacitance of the equivalent capacitor, C, can be calculated using Eq. (3), where k_0 and k_r represent the vacuum and relative permittivity, respectively. Here, d is the distance between the two electrodes, and A is the area covered by the electrodes. Additionally, h_{pzt} and ν denote the thickness and Poisson's ratio of the piezoelectric material, respectively. The term $\bar{k}$ refers to the effective dielectric permittivity, which can be determined under plane-strain assumptions using Eq. (4) [46]. It is worth mentioning that the effect of strain on thickness variation based on the Poisson ratio is negligible.

$$C = k_0 k_r \frac{A}{d} = \frac{\bar{k}A}{h_{pzt}(1-\nu\varepsilon)} \cong \frac{\bar{k}A}{h_{pzt}} \tag{3}$$

$$\bar{k} = k_{33} + \frac{e^2_{33}}{c_{33}} \tag{4}$$

The resistance of PZT is very high and mostly it is dominated by R_L. The current source I_D stands for electrical displacement and is calculated by Eq. (5). Where J_D is current flux which is equal to electrical displacement variation in time and $\bar{e}$ is the effective piezoelectric coefficient. Under thin film plane-strain assumption, the transversal strain $\varepsilon_{22} = 0$ and the effective piezoelectric coefficient can be defined as Eq. (6) [35]:

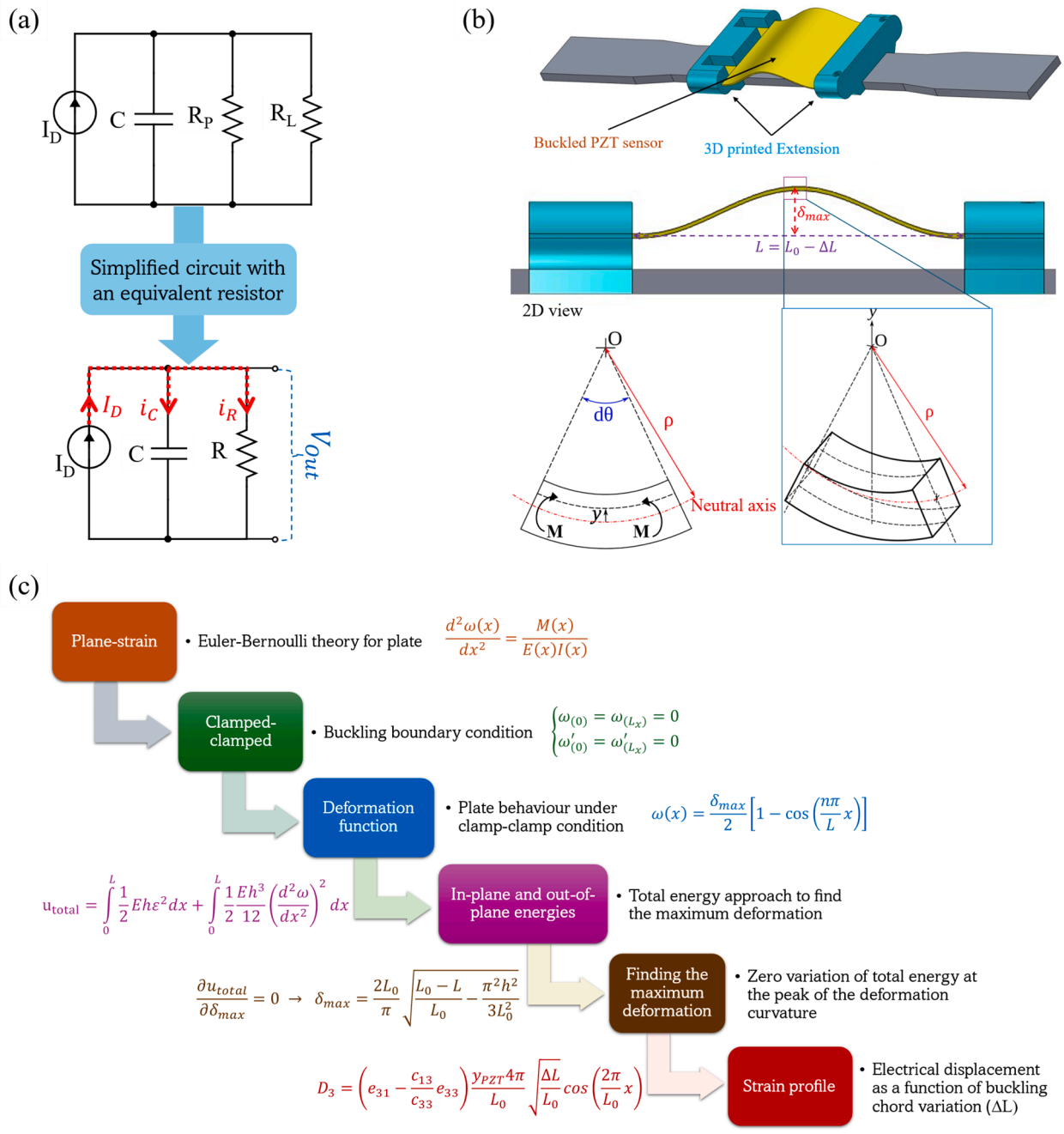

Fig. 2. (a) Equivalent circuit of a piezoelectric sensor in low-frequency range ($f << f_r$) including load resistor and simplified circuit with an equivalent resistor, (b) illustration of the buckled piezoelectric sensor installed on a dog-bone aluminum specimen using the extension, accompanied by a side view and curvature schematic and (c) workflow for strain calculation in a buckled plate.

$$I_D = A \cdot J_D = A \cdot \frac{dD_m(t)}{dt} = A\frac{d\bar{e}\varepsilon(t)}{dt} = A\bar{e}\frac{d\varepsilon(t)}{dt} \tag{5}$$

$$\bar{e} = e_{31} - \frac{c_{13}}{c_{33}}e_{33} \tag{6}$$

Eq. (7) is obtained as a first-order differential equation by identifying all the equivalent circuit components and applying Kirchhoff's Current Law. Eq. (8) is obtained by solving the first-order differential equation in Eq. (7) using the initial condition $V_{(0)}$=0, without requiring additional assumptions or external models.

$$Q = C \cdot V,\ i = \frac{dQ}{dt} \rightarrow i_c = C\frac{dV_{PZT}}{dt} \rightarrow I_D = i_c + i_R = C\frac{dV_{PZT}}{dt} + \frac{V_{PZT}}{R} \tag{7}$$

$$V_{PZT} = \frac{A\bar{e}}{C}e^{-\frac{t}{R \cdot C}}\left(\int \frac{d\varepsilon(t)}{dt}e^{\frac{t}{R \cdot C}}\,dt\right) \tag{8}$$

$\varepsilon_{(t)}$ represents the uniaxial strain of the buckled piezoelectric sensor under dynamic loading, which directly influences the generated voltage as described by Eq. (8). The voltage is proportional to the rate of strain $\varepsilon_{(t)}$, meaning the sensor predominantly measures dynamic strain. Additionally, the time constant, $\tau = RC$, characterizes the sensor's discharge rate or the recombination of generated charge, reflecting the system's tendency to return to equilibrium conditions.

The strain $\varepsilon_{(t)}$ is directly related to the curvature of the sensor or, equivalently, the buckling chord (ΔL), as illustrated in Fig. 2(b) [38]. To establish a correlation between ΔL and $\varepsilon_{(t)}$, an energy-based approach is

employed, with the calculation process outlined in Fig. 2(c). While the boundary conditions significantly influence the buckling behavior, this analytical study assumes a CC configuration which experimentally showed better performance. This choice, as demonstrated later in the results section, proves to be the most optimal for maximizing the sensor's output voltage.

The Euler-Bernoulli theory describes the deformation behavior of the piezoelectric sensor, relying on the key assumption that the plane sections remain plane [47]. This implies that shear deformation across the section is negligible. Additionally, the theory assumes a linear stress distribution, which holds true only if the maximum stress remains below the material's yield stress, as specified in Table 1. To find the relation of strain and physical dimension and the deformation function, let's start with Eq. (9) which correlates the bending moment M and the deformation function of the piezoelectric sensor $\omega_{(x)}$, where (x) indicates that the displacement is applied exclusively along the x-coordinate.

$$\frac{d^2\omega(x)}{dx^2} = \frac{M(x)}{E(x)I(x)} \tag{9}$$

Where E and I represent the modulus of elasticity and the moment of inertia. is the deformation function. As illustrated in the bending schematic in Fig. 2(b), the piezoelectric sensor consists of a symmetric seven-layer structure with the PZT layer positioned at the center (Fig. 1(g)). This placement determines the neutral axis to be at the middle of the PZT layer. Consequently, the amplitude of strain increases linearly with the distance from the neutral axis. Eq. (10) expresses this relationship and incorporates Hooke's law to calculate the resulting stress in the sensor.

$$\varepsilon = \frac{y}{\rho} \rightarrow \sigma = \varepsilon \cdot E = E\frac{y}{\rho} \tag{10}$$

The bending moment M arises from the internal stresses distributed across the cross-sectional area of the element. It relates to the stress distribution as described in Eq. (11).

$$M = \int \sigma . y dA \xrightarrow{\left(\sigma = E\frac{y}{\rho}\right)} M = \frac{E}{\rho}\int y^2 dA \tag{11}$$

The Integral $\int y^2 dA$ represents the moment of inertia I of the cross-section. Thus, $M = \frac{EI}{\rho}$ Considering Eq. (9), the deformation function is related to the bending radius ρ as expressed in Eq. (12).

$$\frac{d^2\omega(x)}{dx^2} = \frac{1}{\rho} \tag{12}$$

As illustrated in the bending schematic in Fig. 2(b), Eq. (13) establishes the relationship between the bending radius, the bending angle, and the chord length (L) of the bent element.

$$L = \rho d\theta \rightarrow L' = (\rho + y)d\theta \xrightarrow{(L=\rho d\theta)} dl = L + yd\theta \text{ then : } yd\theta = L - dl = \Delta L \tag{13}$$

Since strain is $\varepsilon = \frac{\Delta L}{L} = \frac{y}{\rho}$ Eq. (12) can be rewritten as Eq. (14):

$$\varepsilon = \frac{1}{\rho}y = \frac{d^2\omega(x)}{dx^2}\ y \tag{14}$$

In Eq. (14), the strain distribution can be determined once the deformation function is known. To obtain $\omega_{(x)}$, the energy approach outlined in Fig. 2(c) is applied. The Euler-Bernoulli theory, as expressed in Eq. (15), establishes the relationship between the deformation and the load distribution, which in this case corresponds to the uniaxial compressive load N.

$$D\frac{d^4\omega}{dx^4} = -N\frac{d^2\omega}{dx^2} and D = EI \tag{15}$$

The general solution of this differential equation is expressed as a linear combination of terms derived from the roots of the characteristic equation, as shown in Eq. (16).

$$\omega(x) = C_1 + C_2 x + C_3\cos(\alpha x) + C_4\sin(\alpha x) \tag{16}$$

For a plate clamped at both ends, the boundary conditions at $x = 0$ and $x = L_x$ are as follows:

- The displacement $\omega_{(0)} = \omega_{(Lx)} = 0$, indicating no vertical deflection at the clamped edges.
- The slope of the deformation $\omega'_{(0)} = \omega'_{(Lx)} = 0$, reflecting the absence of rotation at the clamped edges.

The mode shapes associated with the eigenvalues are expressed in Eq. (17), representing the characteristic deformation patterns of the plate under buckling.

$$\omega(x) = \frac{\delta_{max}}{2}\left[1 - \cos\left(\frac{n\pi}{L}x\right)\right] \tag{17}$$

In this analysis, n specifies the buckling mode, and for the current case, the first mode is considered ($n = 1$). The maximum deflection, δ_{max}, is determined by analysing the system's equilibrium condition, which balances the total energy contributions from both in-plane and out-of-plane deformations. The process for establishing this equilibrium is outlined in Eq. (18), where h represents the thickness of the sensor.

$$\frac{dN}{dx} = 0 \rightarrow \frac{d}{dx}Eh\varepsilon = 0 \tag{18}$$

The in-plane and out-of-plane components, along with the modulus of elasticity and the geometric properties of the sensor, collectively determine the resulting compressive load. This relationship is expressed mathematically in Eq. (19).

$$\varepsilon = \underbrace{\frac{du}{dx}}_{in-plane} + \frac{1}{2}\underbrace{\left(\frac{d\omega}{dx}\right)^2}_{out-of-plane} \tag{19}$$

By substituting $\omega_{(x)}$ into Eq. (19), the equilibrium condition outlined in Eq. (18) is resolved, yielding the expression presented in Eq. (20).

$$\begin{aligned} \frac{dN}{dx} &= Eh\left\{\frac{d^2u}{dx^2} + \frac{1}{2}\left[\frac{d}{dx}\left(\frac{\delta_{max}}{2}\left[1 - \cos\left(\frac{2\pi}{L}x\right)\right]\right)\right]^2\right\} = 0 \\ \frac{d^2u}{dx^2} &= -2{\delta_{max}}^2\left(\frac{\pi}{L}\right)^3\cos\left(\frac{2\pi}{L}x\right)\sin\left(\frac{2\pi}{L}x\right) \\ u &= \left(\frac{{\delta_{max}}^2\pi}{16L}\right)\sin\left(\frac{4\pi}{L}x\right) - 2{\delta_{max}}^2\left(\frac{\pi}{L}\right)^3 C_1 x + c_2 \end{aligned} \tag{20}$$

For a clamped condition, the boundary conditions $u_{(0)} = 0$ *and* $\int_0^L du = L_0 - L$ are applicable. These conditions are used to derive the in-plane energy component, as expressed in Eq. (21).

$$u = \left(\frac{{\delta_{max}}^2\pi}{16L}\right)\sin\left(\frac{4\pi}{L}x\right) - \left(\frac{L_0 - L}{L_0}\right)x \tag{21}$$

Substituting Eq. (21) into Eq. (19) defines the strain expressed in Eq. (22).

$$\varepsilon = \frac{1}{4}\left(\frac{\delta_{max}\pi}{L_0}\right)^2 - \frac{L_0 - L}{L_0} \tag{22}$$

To account for the buckling length of the sensor and compute the total in-plane energy along its length, an integral over the sensor's length is applied, as shown in Eq. (23). The subscript *IP* is used to distinguish in-plane terms from out-of-plane (OP) components.

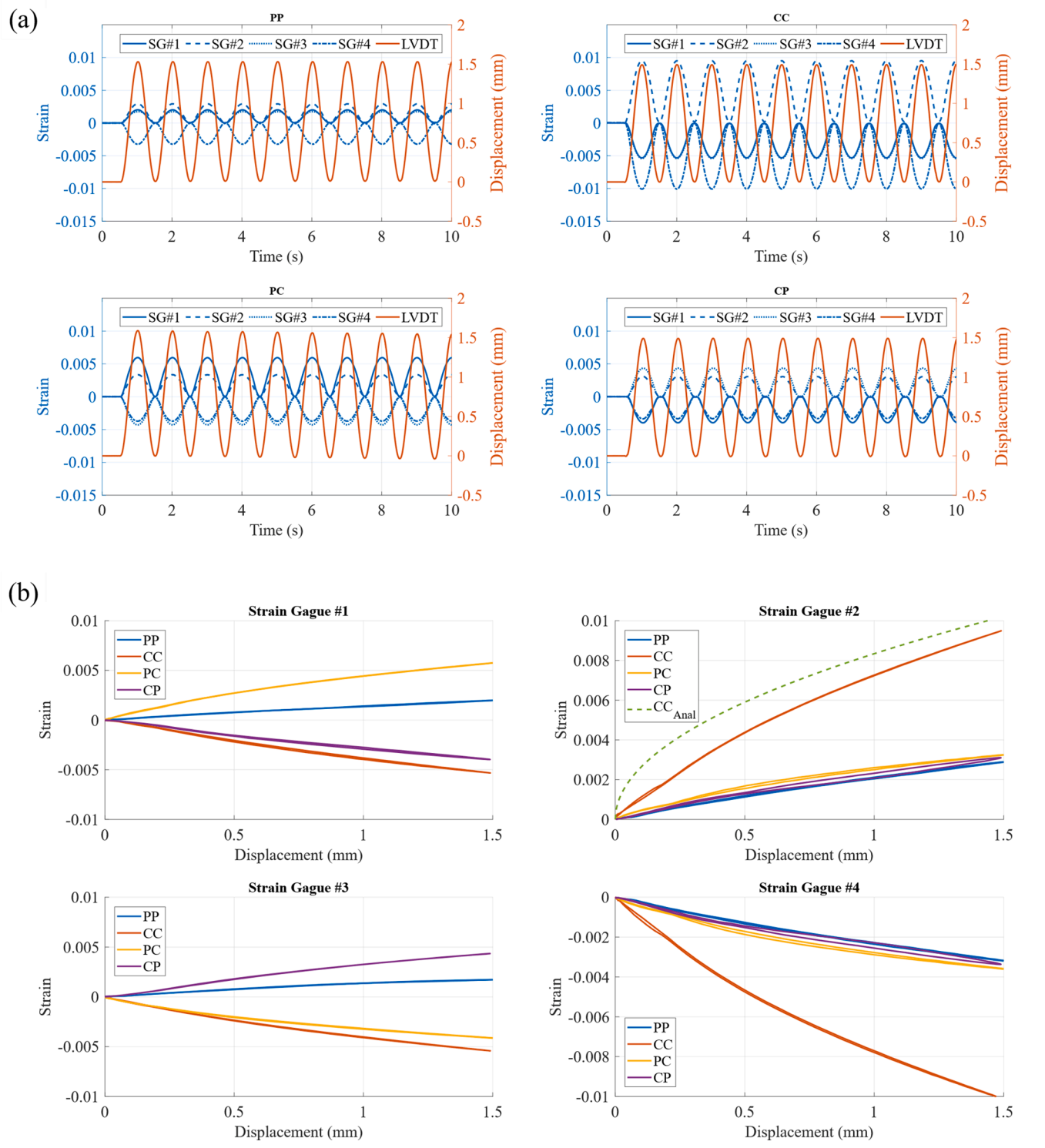

Fig. 3. Strain and buckling chord measurements on different areas of the piezoelectric sensor (a) as a function of time under various boundary conditions and (b) comparison of strain values in different boundary conditions as a function of the buckling chord. CC, CP, PC, and PP refer to clamped–clamped, clamped–pinned, pinned–clamped, and pinned–pinned boundary conditions, respectively.

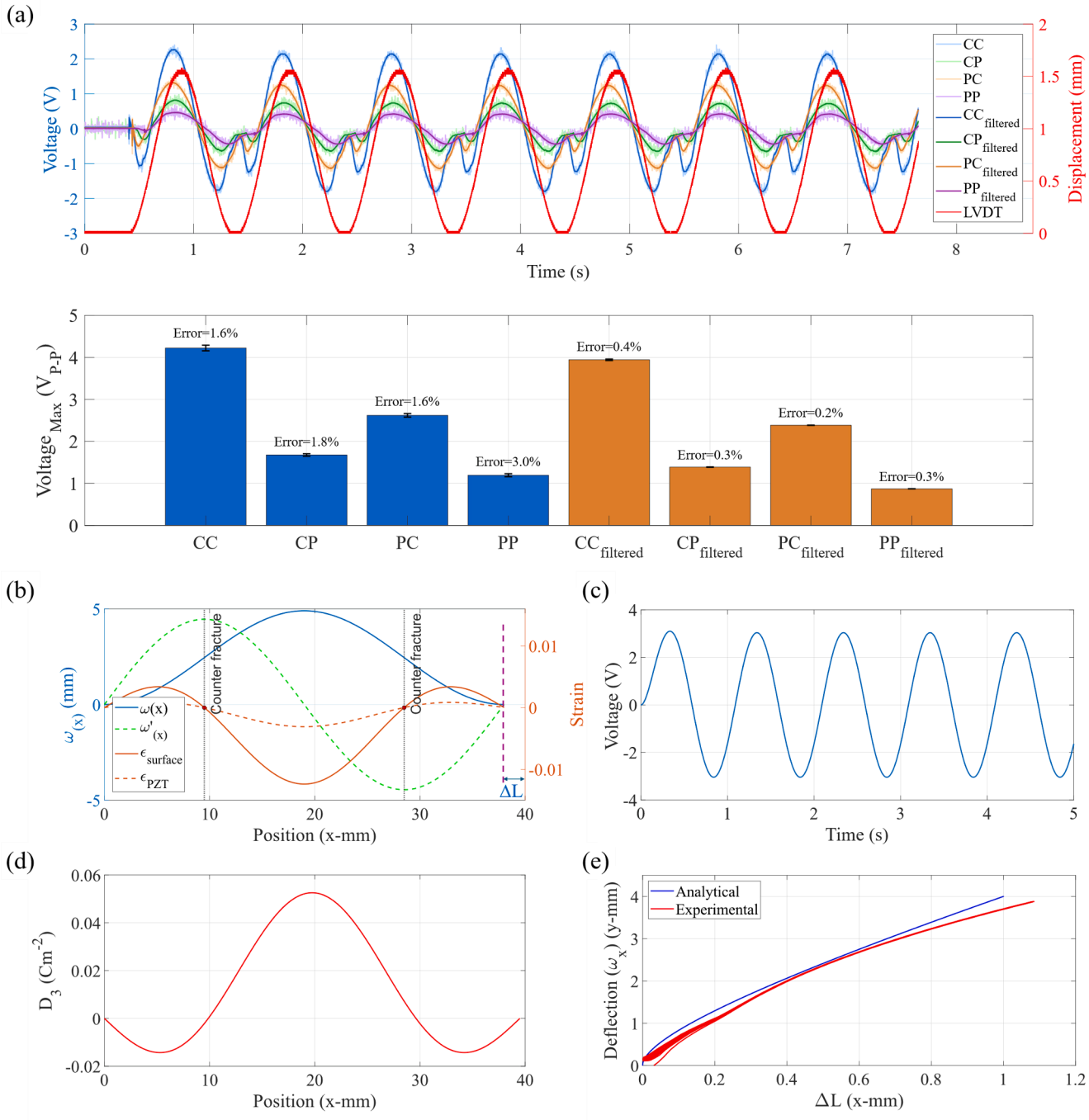

Fig. 4. (a) Comparison of the sensor output under different buckling boundary conditions (pinned and clamped at both ends), alongside the variation in buckling chord measured by an LVDT. Analytical results illustrating: (b) the deformation function and strain distribution on the surface of the piezoelectric sensor and within the PZT layer, (c) the voltage generated by the piezoelectric sensor, (d) the electrical displacement in the PZT layer, and (e) a comparison of the deformation of the piezoelectric sensor as a function of the buckling chord in experiment and analytical studies.

$$u_{IP} = \int_0^L \frac{1}{2} Eh\varepsilon^2 dx$$
$$u_{IP} = Eh\left[\frac{\pi^4 {\delta_{max}}^4}{32L_0^3} - \frac{\pi^2 {\delta_{max}}^2}{4L_0}(L_0 - L)^2 + \frac{(L_0 - L)^2}{L_0}\right] \quad (23)$$

Eq. (24) represents the calculation of the out-of-plane term, accounting for the deformation of the sensor due to buckling.

$$u_{OP} = \int_0^L \frac{1}{2}\frac{Eh^3}{12}\left(\frac{d^2\omega}{dx^2}\right)^2 dx$$
$$u_{OP} = \frac{Eh^3}{12} A {\delta_{max}}^2 \frac{\pi^4}{L^3} \quad (24)$$

To determine the maximum deflection, the variation of the total energy with respect to the curvature slope at the peak of the deformation curvature must equal zero, as shown in Eq. (25).

$$\frac{\partial u_{total}}{\partial \delta_{max}} = \frac{\partial (u_{IP} + u_{OP})}{\partial \delta_{max}} = 0$$
$$u_{total} = \left(\frac{Eh\pi^4}{32L_0^3}\right){\delta_{max}}^4 + \left(\frac{Eh^3\pi^4}{12L_0^2} - \frac{Eh\pi^2(L_0 - L)^2}{4L_0}\right){\delta_{max}}^2 + \frac{Eh(L_0 - L)^2}{L_0}$$
$$\delta_{max} = \frac{2L_0}{\pi}\sqrt{\frac{L_0 - L}{L_0} - \frac{\pi^2 h^2}{3L_0^2}} \quad (25)$$

The deformation function as a function of the buckling chord is represented in Eq. (26).

$$\omega(x) = \frac{L_0}{\pi}\sqrt{\frac{L_0 - L}{L_0} - \frac{\pi^2 h^2}{3L_0^2}}\left[1 - \cos\left(\frac{\pi}{L}x\right)\right] \quad (26)$$

The term $\varepsilon_c = \frac{\pi^2 h^2}{3L_0^2}$ represents the critical buckling strain for Euler buckling in a doubly clamped condition. The sensor buckles when $\frac{L_0 - L}{L_0} > \varepsilon_C$. From Fig. 2(b), the displacement in the buckling chord is $\Delta L = L_0 - L$. When comparing the critical buckling strain with the displacement in the buckling chord, it can be concluded that the critical buckling strain is negligible in comparison to the displacement. By substituting the deformation function into Eq. (14), the strain distribution is represented in Eq. (27).

$$\varepsilon = y\frac{4\pi}{L_0}\sqrt{\frac{\Delta L}{L_0}}\cos\left(\frac{2\pi}{L_0}x\right) \quad (27)$$

This strain is along the x-direction (longitudinal). Since plane strain is assumed, the transverse strains are zero: $\varepsilon_{22} = \varepsilon_{12} = \varepsilon_{23} = 0$ [35]. The strain through the thickness is proportional to the longitudinal strain, as shown in Eq. (28) under the assumption that there is no external applied electric field [37].

$$\varepsilon_{33} = -\frac{c_{13}}{c_{33}}\varepsilon_{11} \quad (28)$$

The strain in each layer of the piezoelectric sensor can be calculated by considering the distance of the layer from the neutral axis, which is located in the middle of the PZT layer (Fig. 1(g)). The strain in the PZT layer contributes to the electrical displacement, and thus, the total electrical displacement for the buckled piezoelectric sensor under the plane strain condition is given by Eq. (29).

$$D_3 = \varepsilon_{11}e_{31} + \varepsilon_{33}e_{33}$$
$$D_3 = \varepsilon_{11}\left(e_{31} - \frac{c_{13}}{c_{33}}e_{33}\right)$$
$$D_3 = \left(e_{31} - \frac{c_{13}}{c_{33}}e_{33}\right)\frac{y_{PZT}4\pi}{L_0}\sqrt{\frac{\Delta L}{L_0}}\cos\left(\frac{2\pi}{L_0}x\right) \quad (29)$$

Substituting Eqs. (27)–29 into Eq. (8) yields Eq. (30), the sensor voltage as a function of the buckling chord. This relationship allows us to express the output voltage of the piezoelectric sensor in terms of the displacement in the buckled sensor, establishing a direct link between the mechanical uniaxial strain in test specimens, such as the dog-bone aluminum shown in Fig. 2(b), and the generated electrical signal.

$$V_{PZT} = \frac{A}{C}e^{-\frac{t}{R\cdot C}}\left\{\int \frac{d}{dt}\left[\left(e_{31} - \frac{c_{13}}{c_{33}}e_{33}\right)\frac{y_{PZT}4\pi}{L_0}\sqrt{\frac{\Delta L}{L_0}}\cos\left(\frac{2\pi}{L_0}x\right)\right]e^{\frac{t}{R\cdot C}}\,dt\right\} \quad (30)$$

Eq. (30) represents the classical exponential decay of voltage across a capacitor in a first-order RC circuit, as commonly found in basic circuit theory [48]. In the context of this study, it describes the transient discharge behaviour of the piezoelectric sensor, where the sensor's intrinsic capacitance and resistance, together with the external resistance, form an effective RC network that governs the transient voltage response

4. Results and discussions

This section presents the experimental evaluation of the developed equations, with a primary focus on validating Eq. (30) and linking experimental observations to the theoretical model for improved sensor design and a more precise voltage-strain correlation. The parameters R and C can be adjusted through external electrical connections, while the strain in the test structure determines **Δ**L. To investigate the influence of boundary conditions, different extension configurations were applied to achieve pinned or clamped conditions at the sensor's ends. Fig. 3(a) shows the strain distribution measured at four distinct locations, as indicated in Fig. 1(f), for the four boundary conditions tested.

As shown in Fig. 3(a), for all the boundary conditions, SG#2 and SG#4 exhibit good symmetry due to being installed at the same axial location on opposite surfaces. Under the CC condition, in addition to displaying higher strain at the top middle point (SG#2), SG#1 and SG#3 indicate the same strain. This is because in the clamped condition, both ends of the PZT-covered area are fixed, causing the side near the electrode connector to stretch more, as indicated in green in Fig. 1(f). However, under the PC and CP conditions, SG#1 and SG#3 do not display the same profile due to the asymmetric position of the PZT and copper electrode layer, which alters the local stiffness across the sensor.

To facilitate a clearer comparison, Fig. 3(b) presents the measured strains as a function of buckling chord variation, confirming the highest strain levels experienced by the CC condition. Additionally, the SGs located on the clamped side's top surface (SG#1 and SG#3) exhibit a negative strain due to the convex curvature. For SG#2 under the CC condition, an analytical solution (Eq. (27)) that accounts for the full sensor thickness is included as a green dashed line. The analytical curve shows a good agreement with the experimental data in both magnitude and curvature, supporting the validity of the model for strain distribution in the buckled configuration.

Although the CC condition shows higher strain at the middle point (SG#2), the strain at SG#1 and SG#3 has the opposite sign, which makes it difficult to determine which boundary condition results in a higher overall strain. However, since strain along the sensor generates electrical displacement, which in turn affects the output voltage, the output voltage can serve as an indicator of the sensor's performance under different boundary conditions. The output voltages from the piezoelectric sensor are shown in Fig. 4(a), with the legend notation using two letters to indicate the boundary condition at each end. A low-pass filter was applied to the measured voltage signals to reduce the high-frequency noise. The buckling process was consistent across all the conditions, transitioning from a flat state to a maximum buckling of 1.5 mm at a frequency of 1 Hz.

Fig. 4(a) demonstrates that the CC boundary condition generates the highest output voltage, while the PP condition produces the lowest and

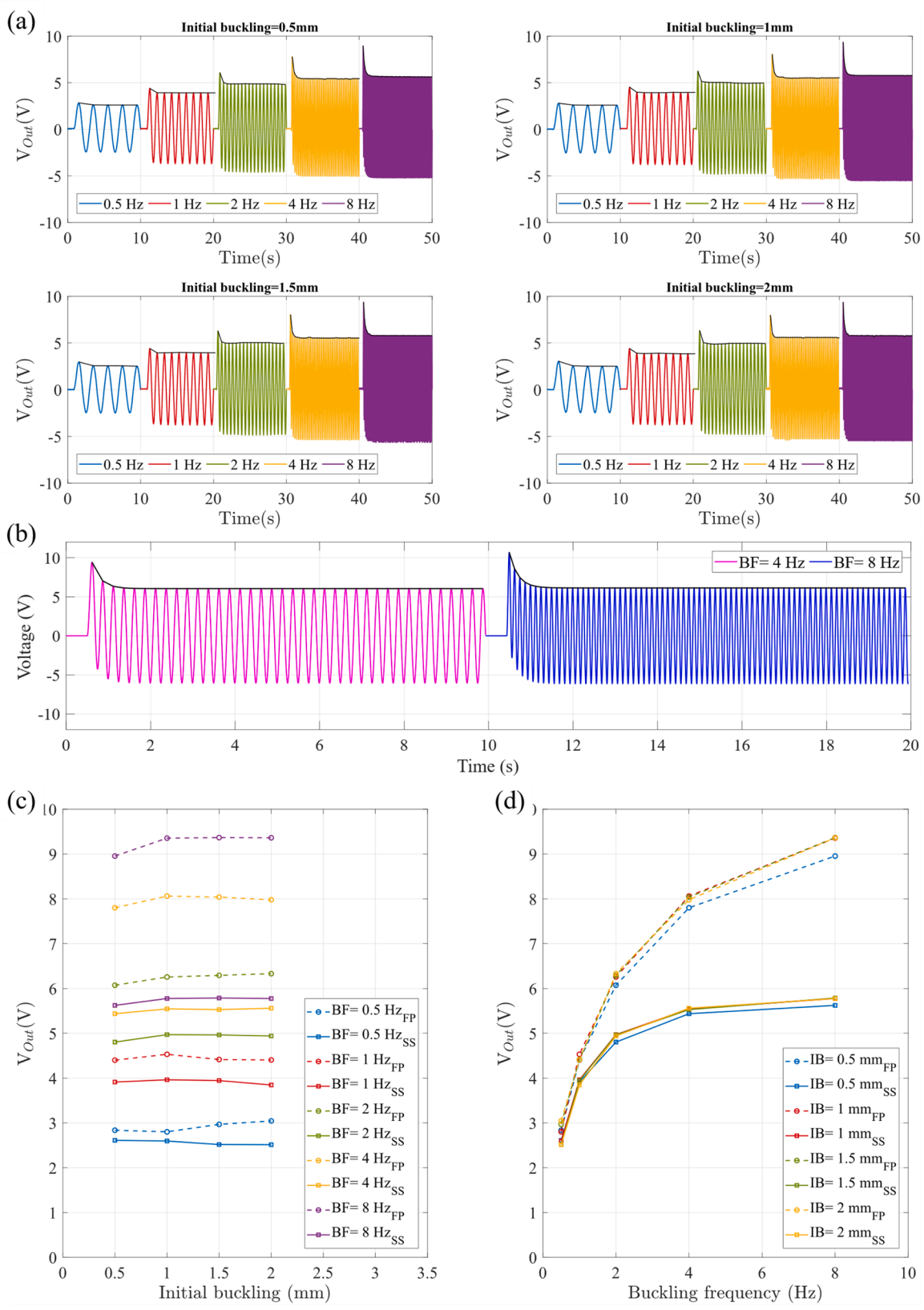

Fig. 5. The output voltage of the piezoelectric sensor under the CC condition, (a) experimental results, showing the variation with BF and different IB chords, (b) analytical results for two different BFs, (c) dependency of output voltage on IB and (d) BF for both transient and SS stages.

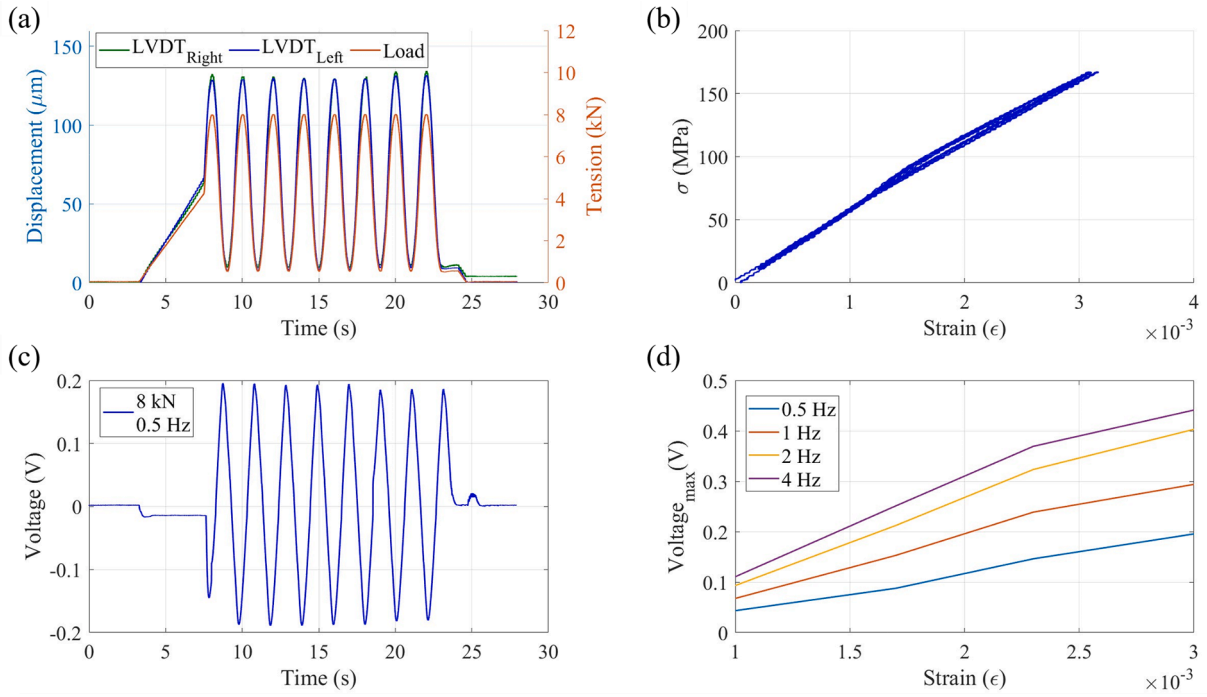

Fig. 6. (a) Applied tensile load and measured displacement between the extension legs, (b) load-strain response of the test structure, (c) generated voltage by the piezoelectric sensor and (d) voltage-strain relationship at different loading frequencies.

the CC condition is a good choice as the most sensitive boundary condition. The difference between the CP and PC conditions arises from the asymmetric clamped length and difference in clamp shape because of electrode connections. Specifically, the side with the electrode connections has more space, resulting in unequal strain distributions under these conditions. Also, Fig. 3(a) shows the strain level in CP is lower than in PC.

Another notable observation is the perturbation in the sensor voltage signal when the displacement, as measured by the LVDT, reaches zero. During the buckling cycle, there is a moment when the LVDT shows no variation as the reciprocating movement transitions in direction. At this point, the piezoelectric sensor tends to discharge due to its inherent capacitance and resistance properties.

To explore further the CC condition, Fig. 4(b-e) provides analytical results for the deformation function, strain distribution, and electrical outputs of the piezoelectric sensor. Fig. 4(b) reveals that the strain distribution along the sensor's length is not uniform in sign. Examining the deformation function shows two convex regions near the ends, which induce compressive strain on the upper surface, and a larger concave region in the middle, resulting in tensile strain on the upper surface. Considering the piezoelectric layer's thickness and its position that is closer to the neutral axis, the strain on the PZT surface (ε_{pxt}) is approximately 25 % of the strain at the top surface. Mathematically, there must be a point where the slope of the deformation function changes the sign as shown by a green dashed line in Fig. 4(b), leading to zero strain—this is referred to as the counter-fracture point.

The electrical displacement in Fig. 4(d) further confirms the strain variation, which reflects strain sign changes. The distance between the two counter-fracture points determines L, leading to a higher strain value. This higher strain in the middle is influenced by the two convex regions near the ends. These regions, being opposite to the concave middle, contribute to an overall strain that remains higher than other boundary conditions. Fig. 4(c) presents the analytically derived voltage, which closely matches the experimental measurements in Fig. 4(a). A key analytical outcome is the maximum deformation, illustrated in Fig. 4(e), which aligns well with the experimental results obtained using the test setup shown in Fig. 1(a).

To address the perturbation issue in the output voltage observed in Fig. 4(a), different IB chords (ranging from 0.5 mm to 2 mm) were applied during the installation of the extensions to prevent the sensor from reaching a fully flat stage. Fig. 5(a) shows the effect of these IB chords on the output voltage. The results indicate that introducing an IB eliminates the voltage perturbation; however, the magnitude of the IB does not significantly affect the output voltage. According to the developed equations, the IB does not influence the output voltage, as it appears in the deformation function but does not contribute directly to the strain rate, which governs the voltage generation.

The voltage signal exhibits both transient and steady-state (SS) responses. As shown in Fig. 5(a), the voltage amplitude is higher during the beginning of buckling but eventually stabilizes to a SS value. This behaviour can be attributed to the time-dependent exponential terms in Eq. (30), which diminish over time and become negligible in the steady state. Fig. 5(b) illustrates the results of Eq. (30) for two BFs, 4 Hz and 8 Hz, confirming this behaviour. Additionally, higher BFs lead to a higher rate of voltage variation as well as an increase in voltage amplitudes. Similarly, the transient time, highlighted by a black line in all graphs in Fig. 5(a and b), is significantly shorter at higher frequencies (e.g., 4 Hz) compared to lower frequencies (e.g., 0.5 Hz).

To further investigate the effect of IB, Fig. 5(c) and 5(d) illustrate how the output voltage depends on both the IB and the buckling frequency (BF). The first peak (FP) represents the maximum value during the transient stage, while the SS value is taken as the average of the subsequent peaks. Fig. 5(c) shows that IB has a negligible influence on the output voltage in both stages. In contrast, Fig. 5(d) demonstrates an exponential-like increase in output voltage with rising BF.

Since the IB level does not significantly affect the output voltage, it is optimal to set the IB based on the strain levels of the test structure. The displacement between the two legs of the extension must not exceed the IB distance; otherwise, the sensor could reach a fully flat state, reintroducing voltage perturbations that could interfere with strain calculations. Additionally, the bending radius must not exceed the minimum bending radius specified in Table 1.

An IB of 1 mm is selected for the test structure, an aluminum dog-bone specimen (Fig. 1(h)). The applied tensile load and the measured

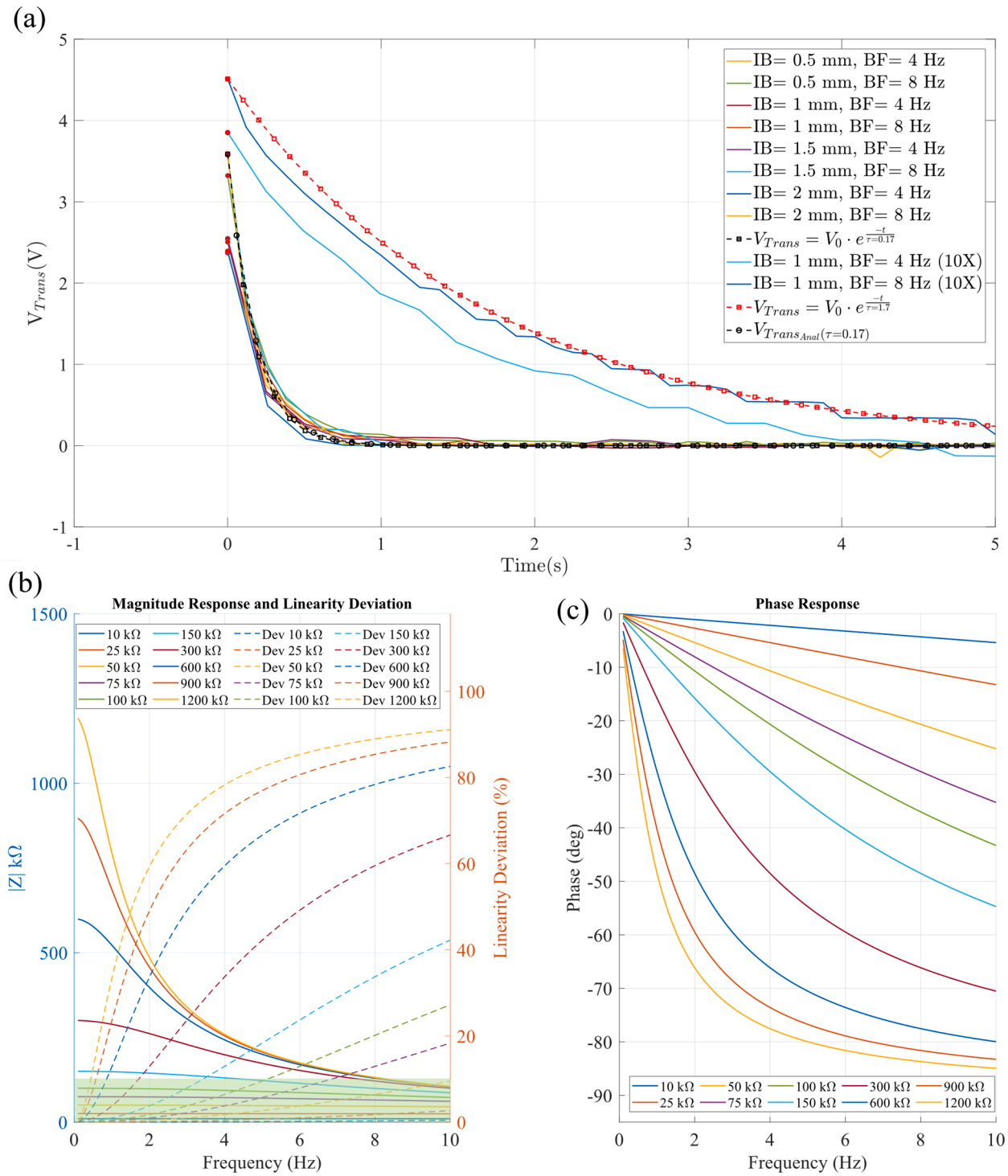

Fig. 7. (a) Experimental and analytical transient response for varying IB and BF, (b) and (c) Bode plots of piezoelectric impedance as a function of externally connected resistance.

displacement between the extension legs are shown in Fig. 6(a). As Fig. 6 (b) illustrates, the applied load remains within the elastic region of the test structure.

The generated voltage from the piezoelectric sensor, shown in Fig. 6 (c), confirms that IB helps mitigate voltage perturbations. During the initial loading stage, which follows a ramp wave, the sensor produces a nearly constant voltage with an initial exponential-like response. This behavior aligns well with Eq. (30), where the constant ramp rate results in a steady voltage, while the exponential terms contribute to the transient response.

Fig. 6(d) presents the voltage-strain relationship across different loading frequencies, showing a linear correlation between voltage and strain for each frequency. However, similar to Fig. 5(d), the voltage does not exhibit a linear dependency on loading frequency. The slight deviation at higher strain levels is attributed to a minor slip of structure in the clamps, causing a lower voltage output.

The nonlinearity observed in the output voltage with respect to BF originates from the capacitive behavior of the piezoelectric sensor. At

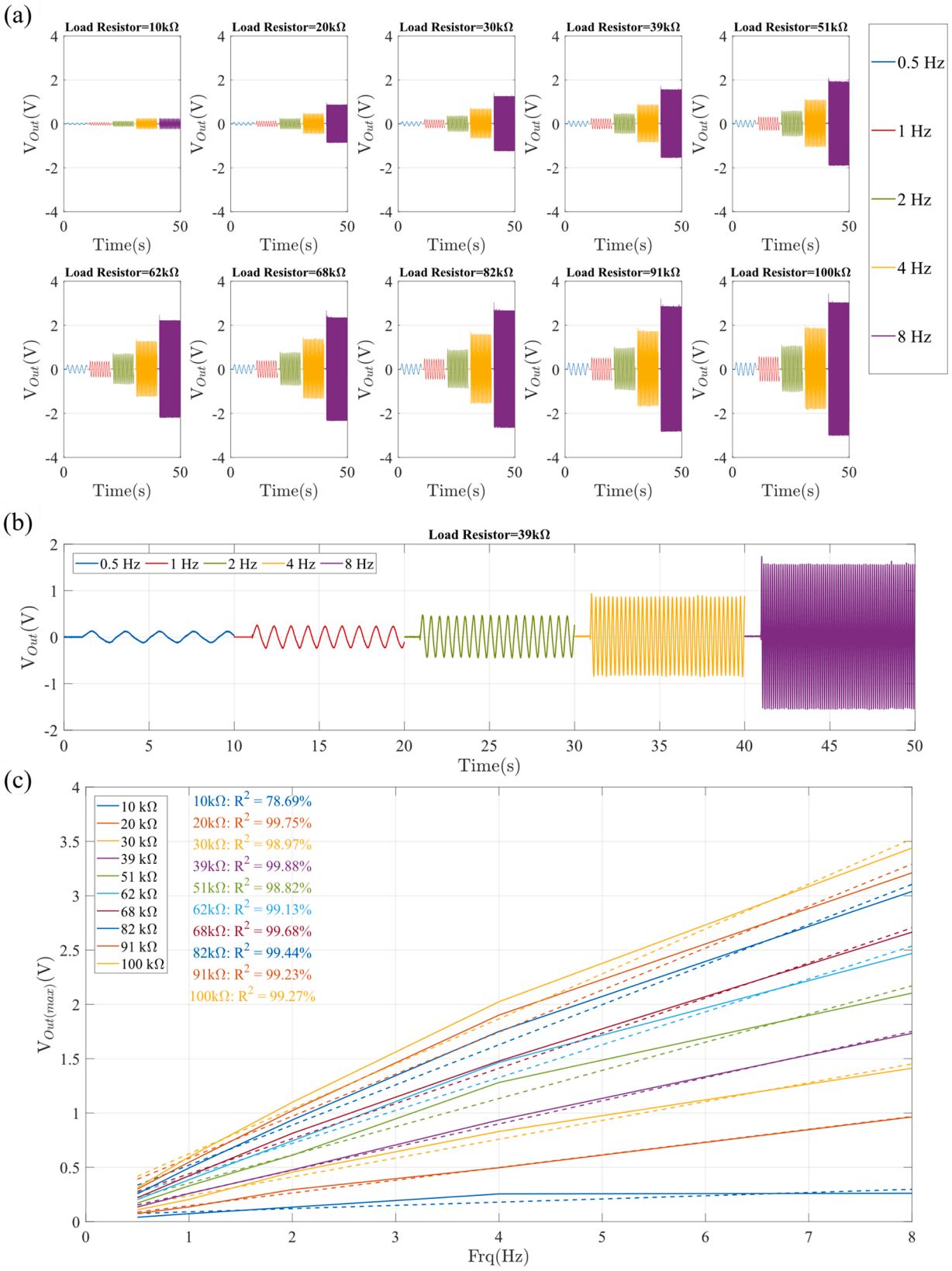

Fig. 8. (a) Output voltage of the piezoelectric sensor with varying external resistances (10 kΩ to 100 kΩ) and BFs (0.5 to 8 Hz), (b) close-up of transient and SS voltages with a 20 kΩ resistor and (c) output voltage dependence on BF for different resistances.

higher frequencies, the generated charges accumulate in the sensor's inherent capacitance (see Fig. 2(a)) but do not have sufficient time to discharge before the load reverses direction. As a result, the system exhibits a smaller effective time constant, which directly affects the transient voltage response [49] as described by the exponential term in Eq. (30).

To quantify the time constant of the piezoelectric sensor, Fig. 7(a) shows the transient output voltage for BFs of 4 Hz and 8 Hz under varying IB conditions. A fitted function of the form $V_0 e^{-\frac{t}{\tau}}$, with $\tau = R{\cdot}C = 0.17\ s$, demonstrates close agreement with the experimental data. Using the known sensor capacitance of 150 nF (Table 1), this corresponds to an estimated internal resistance of approximately 1.13 MΩ.

Since the voltage is recorded via an oscilloscope with a 1 MΩ input impedance, this resistance acts in parallel with the sensor's internal resistance. In such a configuration, the total equivalent resistance is always less than the lowest individual resistor $\left(R_{total} = \frac{R_1 \cdot R_2}{R_1 + R_2}\right)$. Therefore, the observed time constant of 0.17 s implies that the sensor's internal resistance must be higher than 1 MΩ.

To further validate this finding, the experiment was repeated using a 10 MΩ oscilloscope probe at 4 Hz and 8 Hz for 1 mm IB. The resulting transient response, also shown in Fig. 7(a), was best fitted with a function using $\tau = R{\cdot}C = 1.7\ s$. This confirms that the sensor's internal resistance is much greater than 10 MΩ, though it lies beyond the measurable range of a conventional ohmmeter.

To understand how an external resistor influences the piezoelectric impedance, Fig. 7(b) and 7 (c) present Bode plots of the overall impedance for a range of resistances from 10 kΩ to 1.2 MΩ. Both the amplitude and phase of the impedance reveal that higher external resistances lead to increased nonlinearity, which can be connected to the piezoelectric time constant. The green highlighted region in Fig. 7(b) represents the range where the nonlinearity in impedance remains below 10 %, defining an optimal resistance range of up to 50 kΩ. Based on this analysis, if the external resistance is set within the aforementioned range, the dependency of the output voltage on BF becomes significantly more linear. This improvement enhances the strain-voltage relationship, making it more straightforward and less complex to interpret.

To experimentally evaluate the effect of an external resistor on the linearity of the sensor's voltage-BF relationship, a range of resistances from 10 kΩ to 100 kΩ was applied to the piezoelectric sensor under 1 mm of IB and a BF range of 0.5 to 8 Hz. The results are shown in Fig. 8. As illustrated in Fig. 8(a), increasing the external resistance leads to higher output voltage amplitudes, but the transient response is significantly reduced. A closer view in Fig. 8(b), focusing on the results with a 39 kΩ external resistor, highlights that the difference between the FP and the SS stage is minimal and occurs only during the first cycle. Additionally, Fig. 8(c) presents the dependency of output voltage on BF across different external resistances. Dashed lines represent linear regression fits applied to each dataset, and the corresponding coefficient of determination (R^2) values, expressed as percentages, are displayed directly within the figure. These R^2 values quantify the degree of linearity for each resistance. A comparison with Fig. 5(d) reveals a marked improvement in linearity when using optimized external resistors. Notably, the 20 kΩ and 39 kΩ cases exhibit R^2 values above 99.7 %, making them strong candidates for linear strain–voltage conversion. However, this enhancement in linearity comes at the expense of reduced voltage amplitude compared to the results in Fig. 5(d), highlighting a trade-off between output magnitude and frequency-response consistency. Similar linearization trade-offs have been observed in other electromechanical systems, including carbon nanotube (CNT) /cement composites [53] and cementitious sensors [54], where impedance tuning enhanced linear behavior under dynamic loading. Furthermore, FEM modeling of CNT-based materials has demonstrated that nonlinearities in electromechanical response can be mitigated through impedance-aware structural design [55]. These findings support the generalizability of impedance optimization as an effective tool for improving sensor response consistency across material systems.

Compared to prior studies focusing on energy harvesting with buckled piezoelectric films [50–52], this work offers a distinct contribution to dynamic strain sensing. Unlike earlier works which mainly considered fixed boundary conditions (often clamped–clamped), our study systematically compares four boundary configurations and demonstrates that the clamped–clamped condition yields up to 1.65 × higher voltage output and 3 × higher peak strain than others. Moreover, while most previous studies assumed idealized impedance, we show that impedance tuning with external resistors significantly improves voltage linearity (by up to 40 %), especially across varying BFs. Additionally, our custom-designed extension provides a practical solution for integrating the sensor into structures while controlling IB — an installation and repeatability factor not systematically addressed in earlier work.

5. Conclusions

This study explores the use of piezoelectric sensors operating in buckling mode for structural strain measurement, focusing on boundary conditions, sensor response linearity, and impedance optimization. An analytical model supported by experimental validation was developed to establish a comprehensive voltage-strain relationship for dynamic strain monitoring. The developed knowledge can enhance the practical use of piezoelectric sensors in structural strain monitoring, offering greater accuracy, larger measurement range, durability, and installation flexibility. Key findings include:

- Sensor output is highly influenced by boundary conditions, with CC configurations generating the highest voltage due to greater induced strain, highlighting essential considerations for sensor design and installation.
- Output voltage perturbations caused by the sensor's inherent capacitance and resistance, particularly at zero-displacement transitions, were mitigated by introducing IB without compromising performance.
- Sensor output voltage increases with BF due to higher strain rate. The derived time constant from transient response analysis showed strong agreement with experimental data.
- Impedance engineering was found to improve voltage linearity with respect to frequency variation. While this optimization reduces voltage amplitude, it yields a more stable and predictable sensor response—a trade-off that has also been observed in CNT-based and cementitious electromechanical systems.

CRediT authorship contribution statement

Aliakbar Ghaderiaram: Writing – original draft, Visualization, Validation, Software, Methodology, Investigation, Formal analysis, Data curation, Conceptualization. **Erik Schlangen:** Writing – review & editing, Supervision, Resources, Funding acquisition. **Mohammad Fotouhi:** Writing – review & editing, Supervision, Resources, Project administration, Investigation, Formal analysis.

Declaration of competing interest

The authors declare that they have no known competing financial interests or personal relationships that could have appeared to influence the work reported in this paper.

Data availability

Data will be made available on request.

References

[1] D. Shen, D. Pei, T. Ma, Structure strength dynamic strain measurement acquisition system based on data fusion, Sci. Program. 2022 (2022) 9689404, https://doi.org/10.1155/2022/9689404.

[2] Z. He, W. Li, H. Salehi, H. Zhang, H. Zhou, P. Jiao, Integrated structural health monitoring in bridge engineering, Autom. Constr. 136 (2022) 104168, https://doi.org/10.1016/J.AUTCON.2022.104168.

[3] Á. Cunha, E. Caetano, F. Magalhães, C. Moutinho, Dynamic identification and continuous dynamic monitoring of bridges: different applications along bridges life cycle, Struct. Infrastruct. Eng. 14 (2018) 445–467, https://doi.org/10.1080/15732479.2017.1406959.

[4] F. Wang, R. Li, Y. Xiao, Q. Deng, X. Li, X. Song, A strain modal flexibility method to multiple slight damage localization combined with a data fusion technique, Measurement 182 (2021) 109647, https://doi.org/10.1016/J.MEASUREMENT.2021.109647.

[5] E. Copertaro, Assessment of resistive strain gauges measurement performances in experimental modal analysis and their application to the diagnostics of abrasive waterjet cutting machinery, Measurement 188 (2022) 110626, https://doi.org/10.1016/J.MEASUREMENT.2021.110626.

[6] H. Cui, X. Xu, W. Peng, Z. Zhou, M. Hong, A damage detection method based on strain modes for structures under ambient excitation, Measurement 125 (2018) 438–446, https://doi.org/10.1016/J.MEASUREMENT.2018.05.004.

[7] Z. Wang, M. Liu, Z. Zhu, Y. Qu, Q. Wei, Z. Zhou, et al., Clamp looseness detection using modal strain estimated from FBG based operational modal analysis, Measurement 137 (2019) 82–97, https://doi.org/10.1016/J.MEASUREMENT.2019.01.051.

[8] P. Li, Z. Zhang, J. Zhang, Simultaneously identifying displacement and strain flexibility using long-gauge fiber optic sensors, Mech. Syst. Signal. Process. 114 (2019) 54–67, https://doi.org/10.1016/J.YMSSP.2018.05.005.

[9] D. Anastasopoulos, M. De Smedt, L. Vandewalle, G. De Roeck, E.P.B. Reynders, Damage identification using modal strains identified from operational fiber-optic Bragg grating data, Struct. Health Monit. 17 (2018) 1441–1459, https://doi.org/10.1177/1475921717744480/ASSET/IMAGES/LARGE/10.1177_1475921717744480-FIG20.JPEG.

[10] D. Anastasopoulos, G. De Roeck, E.P.B. Reynders, Influence of damage versus temperature on modal strains and neutral axis positions of beam-like structures, Mech. Syst. Signal. Process. 134 (2019) 106311, https://doi.org/10.1016/J.YMSSP.2019.106311.

[11] A. Leal-Junior, M. Silveira, C. Marques, A comparison of temperature compensation methods in a diaphragm-embedded FBG, Results Opt. 14 (2024) 100618, https://doi.org/10.1016/J.RIO.2024.100618.

[12] W. Dang, Z. Li, J. Dan, P. Nan, G. Xin, K.S. Lim, et al., High sensitivity fiber Bragg grating (FBG) sensor based on hollow core silica tube (HCST) sensitization for gas pressure and temperature discrimination, Opt. Fiber Technol. 75 (2023) 103202, https://doi.org/10.1016/J.YOFTE.2022.103202.

[13] V.R. Marrazzo, F. Fienga, M. Riccio, A. Irace, G. Breglio, Multichannel approach for arrayed waveguide grating-based FBG interrogation systems, Sensors 21 (2021) 6214, https://doi.org/10.3390/S21186214. Page 6214 2021;21.

[14] W. Chen, Y. Huang, Advanced three-dimensional graphene-based piezoresistive sensors in wearable devices, J. Phys. Conf. Ser. 2174 (2022) 012019, https://doi.org/10.1088/1742-6596/2174/1/012019.

[15] J. He, Y. Zhang, R. Zhou, L. Meng, C. Pan, W. Mai, et al., Recent advances of wearable and flexible piezoresistivity pressure sensor devices and its future prospects, J. Mater. 6 (2020) 86–101, https://doi.org/10.1016/J.JMAT.2020.01.009.

[16] S. Huang, Y. Guo, P. Huo, Q. Li, Redefining vibration sensing: ai-driven analytics, self-powered systems, and multi-modal fusion - a review, IEEe Sens. J. (2025), https://doi.org/10.1109/JSEN.2025.3579345.

[17] M. Liu, Z. Wang, P. Jiang, G. Yan, Temperature compensation method for piezoresistive pressure sensors based on gated recurrent unit, Sensors 24 (2024) 5394, https://doi.org/10.3390/S24165394. Page 5394 2024;24.

[18] M. Sol-Sánchez, J.M. Castillo-Mingorance, F. Moreno-Navarro, Rubio-Gámez MC, Smart rail pads for the continuous monitoring of sensored railway tracks: sensors analysis, Autom. Constr. 132 (2021) 103950, https://doi.org/10.1016/J.AUTCON.2021.103950.

[19] S. Du, J. Zhou, F. Li, Dynamic deformation monitoring of cantilever beams using piezoelectric sensors: theory and experiment, Measurement 227 (2024) 114305, https://doi.org/10.1016/J.MEASUREMENT.2024.114305.

[20] C. Dagdeviren, P. Joe, O.L. Tuzman, Park K Il, K.J. Lee, Y. Shi, et al., Recent progress in flexible and stretchable piezoelectric devices for mechanical energy harvesting, sensing and actuation, Extreme Mech. Lett. 9 (2016) 269–281, https://doi.org/10.1016/J.EML.2016.05.015.

[21] A. Ghaderiaram, E. Schlangen, M. Fotouhi, Structural fatigue life monitoring with piezoelectric-based sensors: fundamentals, current advances, and future directions, Sensors 25 (2025) 334, https://doi.org/10.3390/S25020334. Page 334 2025;25.

[22] A. Aabid, M.A. Raheman, Y.E. Ibrahim, A. Anjum, M. Hrairi, B. Parveez, et al., A systematic review of piezoelectric materials and energy harvesters for industrial applications, Sensors 21 (2021) 4145, https://doi.org/10.3390/S21124145. Page 4145 2021;21.

[23] D. Singh Aulakh, S. Bhalla, Piezo sensor-based operational strain modal analysis of structures: transition from lab to field application, Measurement 239 (2025) 115398, https://doi.org/10.1016/J.MEASUREMENT.2024.115398.

[24] Y.K. An, M.K. Kim, H. Sohn, Piezoelectric transducers for assessing and monitoring civil infrastructures, Sens. Technol. Civ. Infrastruct. 1 (2014) 86–120, https://doi.org/10.1533/9780857099136.86.

[25] Rupitsch S.J. Piezoelectric sensors and actuators 2019. https://doi.org/10.1007/978-3-662-57534-5.

[26] A. Ghaderiaram, N. Vafa, E. Schlangen, M. Fotouhi, Piezoelectric sensor characterization for structural strain measurements, Sens. Actuators Phys. 3 (2025) 116659, https://doi.org/10.1016/j.sna.2025.116659.

[27] C. Wallbrink, J.M. Hughes, A. Kotousov, Application of an advanced piezoelectric strain sensor for crack closure measurement, Int. J. Fatigue 167 (2023) 107286, https://doi.org/10.1016/J.IJFATIGUE.2022.107286.

[28] J. Sirohi, I. Chopra, Fundamental Understanding of Piezoelectric Strain Sensors. https://doi.org/10.1106/8BFB-GC8P-XQ47-YCQ0, 2000.

[29] K.L. Ganapathi, M. Rath, R. Rao, G. Youssef, M. Lopez, S. Newacheck, et al., Temperature-dependent mechanical depolarization of ferroelectric ceramics, J. Phys. D. Appl. Phys. 43 (2010) 175501, https://doi.org/10.1088/0022-3727/43/17/175501.

[30] Y. Chen, S. Xie, Q. Wang, L. Fu, R. Nie, J. Zhu, Correlation between microstructural evolutions and electrical/mechanical behaviors in Nb/Ce co-doped Pb (Zr0.52Ti0.48)O3 ceramics at different sintering temperatures, Mater. Res. Bull. 94 (2017) 174–182, https://doi.org/10.1016/J.MATERRESBULL.2017.05.045.

[31] Q. Huang, Y. Jiang, Z. Duan, Y. Wu, Z. Yuan, J. Guo, et al., Ion gradient induced self-powered flexible strain sensor, Nano Energy 126 (2024) 109689, https://doi.org/10.1016/J.NANOEN.2024.109689.

[32] Z. Yuan, H. Li, Z. Duan, Q. Huang, M. Zhang, H. Zhang, et al., High sensitivity, wide range and waterproof strain sensor with inner surface sensing layer for motion detection and gesture reconstruction, Sens. Actuators Phys. 369 (2024) 115202, https://doi.org/10.1016/J.SNA.2024.115202.

[33] Q. Huang, Y. Jiang, Z. Duan, Z. Yuan, Y. Wu, J. Peng, et al., A finger motion monitoring glove for hand rehabilitation training and assessment based on gesture recognition, IEEe Sens. J. 23 (2023) 13789–13796, https://doi.org/10.1109/JSEN.2023.3264620.

[34] A. Ghaderiaram, E. Schlangen, M. Fotouhi, Analysis of PZT piezoelectric sensors in buckling mode for, E-J. Nondestruct. Test. (2024) 1–8, https://doi.org/10.58286/29596.

[35] C. Dagdeviren, B.D. Yang, Y. Su, P.L. Tran, P. Joe, E. Anderson, et al., Conformal piezoelectric energy harvesting and storage from motions of the heart, lung, and diaphragm, Proc. Natl. Acad. Sci. U S.A 111 (2014) 1927–1932, https://doi.org/10.1073/PNAS.1317233111/SUPPL_FILE/SM04.WMV.

[36] F. Cottone, L. Gammaitoni, H. Vocca, M. Ferrari, V. Ferrari, Piezoelectric buckled beams for random vibration energy harvesting, Smart. Mater. Struct. 21 (2012), https://doi.org/10.1088/0964-1726/21/3/035021.

[37] J. Chen, N. Nabulsi, W. Wang, J.Y. Kim, M.K. Kwon, J.H Ryou, Output characteristics of thin-film flexible piezoelectric generators: a numerical and experimental investigation, Appl. Energy 255 (2019) 113856, https://doi.org/10.1016/J.APENERGY.2019.113856.

[38] J. Song, Y. Huang, J. Xiao, S. Wang, K.C. Hwang, H.C. Ko, et al., Mechanics of noncoplanar mesh design for stretchable electronic circuits, J. Appl. Phys. 105 (2009), https://doi.org/10.1063/1.3148245.

[39] A. Ghaderiaram, R. Mohammadi, E. Schlangen, M. Fotouhi, Development of an innovative extension for fatigue life monitoring using a piezoelectric sensor, Procedia Struct. Integr. 52 (2024) 570–582, https://doi.org/10.1016/J.PROSTR.2023.12.057.

[40] DuraAct™-Piezoelectric Patch Transducers for Industry and Research (2015).

[41] M. Krommer, P. Berik, Y. Vetyukov, A. Benjeddou, Piezoelectric d 15 shear-response-based torsion actuation mechanism: an exact 3D Saint-Venant type solution, Int. J. Smart. Nano Mater. 3 (2012) 82–102, https://doi.org/10.1080/19475411.2011.649807.

[42] O. Scott-Emuakpor, T. George, C. Cross, M.H.H. Shen, Hysteresis-loop representation for strain energy calculation and fatigue assessment, J. Strain Anal. Eng. Des. 45 (2010) 275–282, https://doi.org/10.1243/03093247JSA602.

[43] Cain M.G., Stewart M. Standards for piezoelectric and ferroelectric ceramics 2014: 267–75. https://doi.org/10.1007/978-1-4020-9311-1_12.

[44] M.J. Guan, W.H. Liao, On the equivalent circuit models of piezoelectric ceramics, Ferroelectrics. 386 (2009) 77–87, https://doi.org/10.1080/00150190902961439.

[45] V.T. Rathod, A Review of Electric Impedance Matching Techniques for Piezoelectric Sensors, Actuators Transducers. Electron. 8 (2019) 169, https://doi.org/10.3390/ELECTRONICS8020169. Page 169 2019;8.

[46] J. Chen, N. Nabulsi, W. Wang, J.Y. Kim, M.K. Kwon, J.H Ryou, Output characteristics of thin-film flexible piezoelectric generators: a numerical and experimental investigation, Appl. Energy 255 (2019) 113856, https://doi.org/10.1016/j.apenergy.2019.113856.

[47] A. Öchsner, Euler–bernoulli beam theory, Class. Beam Theor. Struct. Mech. (2021) 7–66, https://doi.org/10.1007/978-3-030-76035-9_2.

[48] Razavi Behzad. Fundamentals of microelectronics : with robotics and bioengineering applications 2021:12.

[49] M.J. Guan, W.H. Liao, On the equivalent circuit models of piezoelectric ceramics, Ferroelectrics. 386 (2009) 77–87, https://doi.org/10.1080/00150190902961439.

[50] C. Dagdeviren, B.D. Yang, Y. Su, P.L. Tran, P. Joe, E. Anderson, et al., Conformal piezoelectric energy harvesting and storage from motions of the heart, lung, and diaphragm, Proc. Natl. Acad. Sci. U S.A 111 (2014) 1927–1932, https://doi.org/10.1073/PNAS.1317233111/SUPPL_FILE/SM04.WMV.

[51] F. Cottone, L. Gammaitoni, H. Vocca, M. Ferrari, V. Ferrari, Piezoelectric buckled beams for random vibration energy harvesting, Smart. Mater. Struct. 21 (2012), https://doi.org/10.1088/0964-1726/21/3/035021.

[52] J. Chen, N. Nabulsi, W. Wang, J.Y. Kim, M.K. Kwon, J.H Ryou, Output characteristics of thin-film flexible piezoelectric generators: a numerical and experimental investigation, Appl. Energy 255 (2019) 113856, https://doi.org/10.1016/J.APENERGY.2019.113856.

[53] B. Han, K. Zhang, X. Yu, E. Kwon, J. Ou, Electrical characteristics and pressure-sensitive response measurements of carboxyl MWNT/cement composites, Cem. Concr. Compos. 34 (2012) 794–800, https://doi.org/10.1016/J.CEMCONCOMP.2012.02.012.

[54] D.A. Triana-Camacho, D.A. Miranda, E. García-Macías, O.A. Mendoza Reales, J. H Quintero-Orozco, Effective medium electrical response model of carbon nanotubes cement-based composites, Constr. Build. Mater. 344 (2022) 128293, https://doi.org/10.1016/J.CONBUILDMAT.2022.128293.

[55] E. García-Macías, R. Castro-Triguero, A. Sáez, F. Ubertini, 3D mixed micromechanics-FEM modeling of piezoresistive carbon nanotube smart concrete, Comput. Methods Appl. Mech. Eng. 340 (2018) 396–423, https://doi.org/10.1016/J.CMA.2018.05.037.